

Pulsed laser deposition films from a $\text{Ba}_2\text{FeMoO}_6$ target onto $\text{SrTiO}_3[001]$: Chemical and magnetic inhomogeneity

Daniel M. Pajerowski, Lisa J. Kraye, Brian J. Kirby, Brian B. Maranville, Julie A. Borchers, Kyeong-Won Kim, and David P. Norton

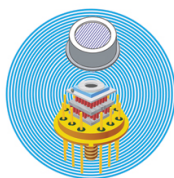
Citation: *Journal of Applied Physics* **124**, 163903 (2018); doi: 10.1063/1.5039401

View online: <https://doi.org/10.1063/1.5039401>

View Table of Contents: <http://aip.scitation.org/toc/jap/124/16>

Published by the *American Institute of Physics*

Ultra High Performance SDD Detectors



See all our XRF Solutions

Pulsed laser deposition films from a $\text{Ba}_2\text{FeMoO}_6$ target onto $\text{SrTiO}_3[001]$: Chemical and magnetic inhomogeneity

Daniel M. Pajerowski,^{1,2} Lisa J. Krayner,² Brian J. Kirby,² Brian B. Maranville,² Julie A. Borchers,² Kyeong-Won Kim,³ and David P. Norton³

¹Neutron Scattering Division, Oak Ridge National Laboratory, Oak Ridge, Tennessee 37831, USA

²NIST Center for Neutron Research, National Institute of Standards and Technology, Gaithersburg, Maryland 20899-6102, USA

³Department of Materials Science and Engineering, University of Florida, Gainesville, Florida 32611, USA

(Received 7 May 2018; accepted 28 September 2018; published online 22 October 2018)

Pulsed laser deposition films from $\text{Ba}_2\text{FeMoO}_6$ (BFMO) targets onto $\text{SrTiO}_3[001]$ (STO) substrates have been reported previously to have non-zero magnetism at 300 K, a majority of magnetic ordering at 240 K that is less than the 370 K ordering temperature of polycrystalline BFMO, and suppressed saturation magnetization compared to polycrystalline BFMO. To interrogate these previously reported observations of BFMO on STO, we have used a combination of x-ray diffraction, atomic force microscopy, x-ray and neutron reflectivity, and x-ray photoelectron spectroscopy that shows inhomogeneities. The present results show off-stoichiometry on the A-site by incorporation of Sr from the substrate and on the B-site to have $\% \text{Fe}/\% \text{Mo} > 1$ by evolution of BaMoO_4 . There is an enhanced ordering temperature and magnetic response nearer to the SrTiO_3 interface compared to the air interface. Depth dependent strain and microstructure are needed to explain the magnetic response. Holistic considerations and implications are also discussed. *Published by AIP Publishing.* <https://doi.org/10.1063/1.5039401>

I. INTRODUCTION

This paper focuses on $\text{Ba}_2\text{FeMoO}_6$ (BFMO) films, as BFMO is a magnetoresistive half-metal that retains this function at room temperature because the magnetic ordering temperature (T_C) can be as high as 367 K.¹ Half-metal ferromagnets like BFMO are of theoretical interest and also have clear application potential in magneto-optics and spintronics.² Moreover, polycrystalline ceramics of BFMO have reported magnetoresistances of greater than 30%.^{3,4} For incorporation in devices, thin films are required, and BFMO films have reduced T_C and saturation magnetization (M_{SAT}) compared to polycrystalline samples.⁵ The lack of explanation for the observed differences between BFMO films on SrTiO_3 (STO) and BFMO powders is a hard limit to applications of BFMO and is the impetus of this work.

More broadly, BFMO is a double perovskite (DP) of the Elpasolite⁶ motif for which the general formula is written as $\text{A}_2\text{BB}'\text{O}_6$ and consists of two interpenetrating perovskite ($\text{ABO}_3/\text{AB}'\text{O}_3$) sublattices, whereby there is a three dimensional chemical ordering of the B and B' species that doubles the $\approx 4 \text{ \AA}$, perovskite unit cell in all three Cartesian directions. By utilizing a combination of 3d and 4d or 5d ions on the B/B' sites, DPs can have contributions of itinerant and localized magnetism. Aside from BFMO, DPs may present unusual magnetotransport, ferroelectric, and magnetic properties that expand upon the already diverse perovskite materials.⁷

The BFMO is similar to the more intensely studied $\text{Sr}_2\text{FeMoO}_6$ (SFMO) that boasts a higher $T_C = 420 \text{ K}$, but a smaller magnetoresistance.⁸ The SFMO sparked interest because of the room temperature magnetoresistance, and the translation to thin film geometries shows a strong potential for device applications.⁹ The naïve estimate of $M_{\text{SAT}} = 4 \mu_B/\text{f.u.}$

for antiparallel alignment of more localized Fe^{3+} ($5 \mu_B$) and more itinerant Mo^{5+} ($1 \mu_B$) in these materials is never fully achieved in polycrystals due to the defects and the breakdown of this simple picture,¹⁰ and both T_C and M_{SAT} are typically less in thin films compared to polycrystals.^{11,12} Two defects that may be present in DPs are anti-site, whereby the chemical order of B and B' is imperfect and off-stoichiometry of the B and B' sites ($\text{A}_2\text{B}_{1+x}\text{B}'_{1-x}\text{O}_6$ where $x=[0,1]$).^{13,14} In addition, the usual off-stoichiometry possible in perovskites, quantified typically by oxygen content,¹⁵ may also affect the behavior of DPs.

Aside from synthesis subtleties, films may be subject to strain at the interface with the substrate due to lattice mismatches. Polarized neutron reflectometry (PNR) is useful to probe the magnetization depth profile and search for correlations with interface effects.¹⁶ Previously, PNR has been used to understand the strain-induced interface effects in the DP $\text{Sr}_2\text{CrReO}_6$ (SCRO).¹⁷ Here, we apply PNR to the BFMO thin films. For the BFMO films on SrTiO_3 (STO) via pulsed laser deposition (PLD), there is a strange feature whereby there is a clear inflection point in the magnetization at around 250 K, which gives rise to $M_{\text{SAT}} = 1.2 \mu_B$ for the optimal growth condition, but above this putative T_C , there is still a ferromagnetic response at 300 K that has $M_{\text{SAT}} = 0.4 \mu_B$ for the optimized growth condition.⁵ One hypothesis of this study is that there may be different magnetic contributions as a function of depth in the BFMO target films deposited on STO (BFMO//STO) that may be probed by PNR.

Following this introduction, the technical details are described in Sec. II. Section III presents our results of X-ray diffraction (XRD), atomic force microscopy (AFM), X-ray reflectivity (XRR), PNR, and X-ray photoelectron

spectroscopy (XPS). These results are discussed in Sec. IV to generate a model of the magnetism and stoichiometry in the PLD BFMO//STO and summarized in the concluding Sec. V.

II. TECHNICAL DETAILS

Films were deposited following the reported procedure of PLD for $\text{Ba}_2\text{FeMoO}_6$ on SrTiO_3 ,⁵ with a variation in the repetition rate and total time in order to tune the film thickness. Four films were prepared for this report, with identifiers assigned as per Table I.

The XPS was collected on a Kratos AXIS Ultra DLD spectrometer equipped with a monochromatic Al source (1486.6 eV) operating at 140 W under a vacuum of 1×10^{-8} Torr. Survey scans were used for better signal to noise when quantifying elemental compositions, and region scans were used for higher resolution to quantify peak splittings. In region scans, the pass energy of the analyzer was set at 20 eV using an energy step size of 0.05 eV, while survey scans used an analyzer pass energy of 160 eV with a step size of 1 eV. The C 1s peak of the adventitious carbon was set to 284.8 eV as a point of reference. Relative sensitivity factors provided with the instrument were used for elemental analysis. Shirley backgrounds were used, and peaks were fit to pseudo-Voigt functions.

Specular XRD experiments were performed on a Rigaku Ultima III Analytical X-Ray Diffractometer with a $2\theta/\theta$ design from $2\theta = 10^\circ$ to 150° using a copper anode. This XRD setup has $\text{Cu-K}_{\alpha 1}$ ($\lambda = 1.5406 \text{ \AA}$) and $\text{Cu-K}_{\alpha 2}$ ($\lambda = 1.5444 \text{ \AA}$) radiations, with the typical Cu-K_{α} satellite ($\lambda = 1.5345 \text{ \AA}$) as well as a contamination of W-L_{α} ($\lambda = 1.4704 \text{ \AA}$).^{18,19} The off-specular XRD reciprocal space maps were measured with a Bruker D8 Advance diffractometer using a copper anode.

AFM of films was scanned using an Asylum Cypher High Resolution Atomic Force Microscope multimode scanning probe microscope with the tapping mode. The images were quantified with the Gwyddion software.²⁰

XRR experiments were performed on a Bruker D8 Advance diffractometer using a copper anode and a Sol-X detector. Specular reflectivity data were taken with the detector angle equal to the incident beam angle and an attenuator was used for positions near and below the critical edge when the reflected intensity was at maximum.

PNR was performed on the PBR ($\lambda = 4.75 \text{ \AA}$) and the MAGIK ($\lambda = 5.00 \text{ \AA}$) reflectometers at the NIST Center for Neutron Research.²¹ The magnetic field of 0.8 T is in the plane of the film.

XRR and PNR data were reduced to a reflectivity profile and corrected for the footprint using reflred in the reflpak suite.²² Profile fitting was performed using the Refl1D

software package, with the DREAM and differential evolution algorithms that attempt to avoid local minima in parameter space.²³ The fitting algorithm in Refl1D, by way of a Monte Carlo Markov-Chain based optimization, allows for parameter uncertainty estimation via the standard deviation (σ_{STD}) of the tested cases, and $n = 1000$ test cases were used in all fits. For reference, $1\sigma_{\text{STD}}$ is the 68% confidence interval, $1.96\sigma_{\text{STD}}$ is the 96% confidence level, and $2.58\sigma_{\text{STD}}$ is the 99% confidence level. For fit comparison of the magnetic contribution, a parameter to track the uncertainty in the spin-asymmetry $U_{\text{SA}} = \Sigma(|S_{\text{A,obs}} - S_{\text{A,calc}}|) / \Sigma |S_{\text{A,obs}}|$ is used, where SA is the spin asymmetry. Due to the many orders of magnitude over which the reflectivity varies, and the nuclear and magnetic contributions for PNR, χ^2 is less sensitive to the details of the magnetic model. Throughout, the momentum transfer Q_z is normal to the plane of the film.

III. RESULTS

A. X-ray diffraction

XRD was used to probe the crystallinity of the BFMO and to extract unit cell parameters of films **i**, **ii**, **iii**, and **iv**. XRD with the momentum transfer perpendicular to the plane of the film showed intense beams from the 00L peaks of the STO substrate, with significantly smaller BFMO peaks on the lower-angle, larger-d-spacing side. The most intense BFMO peak is that related to the STO 002, shown in Fig. 1(a). This peak was seen to increase in intensity with deposition cycles while changing the spacing between B and B' double perovskite sites $d_{\text{BB}'}$, Table II. The precision of the x-ray diffractometer is estimated to be better than 10^{-4} , while a deconvolution of the resolution function of the instrument

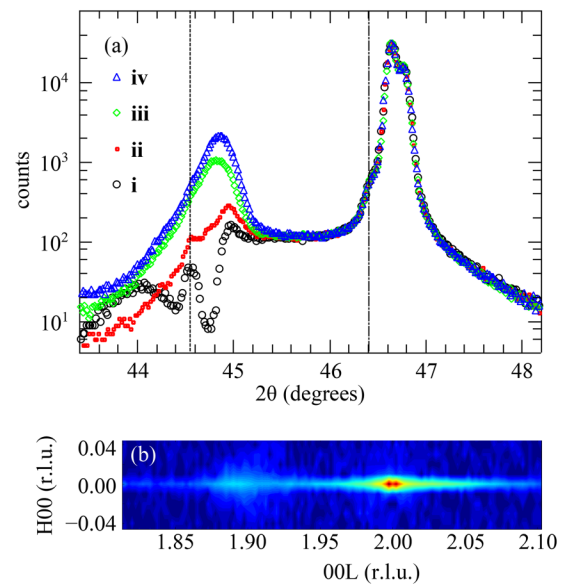


FIG. 1. XRD. (a) A locked-coupled, θ - 2θ region scan shows the substrate with the film peak on the low angle side of the STO 002 peaks ($\text{Cu-K}_{\alpha 1}$ + $\text{Cu-K}_{\alpha 2}$). The STO 002 Cu-K_{α} satellite peak is marked by a vertical dotted line and the STO 002 W-L_{α} peak is marked by a vertical dashed line. The temperature is ambient. (b) An out-of-plane reciprocal space map of sample **i** in reciprocal lattice units indexed to STO, where the intensity is shown on a rainbow scale having red most intense. The temperature is ambient.

TABLE I. Film growth conditions.

Sample ID	Condition	Deposition cycles
i	1 Hz 15 min	900
ii	1 Hz 60 min	3600
iii	3 Hz 60 min	10 800
iv	5 Hz 60 min	18 000

TABLE II. XRD of BFMO//STO.

Sample ID	004 _{BFMO} peak intensity (X-ray counts)	d_{BB} (Å)
i	45	4.030
ii	165	4.034
iii	930	4.044
iv	2030	4.041

suggests an additional broadening in the films due to either finite size or strain. Peak positions were found by least squares fitting of Gaussian functions with fitting uncertainties less than ± 0.0004 Å for the peak center. For films **i** and **ii**, Laue oscillations were observed ($\Delta Q = 2\pi/Na$ for “N” repeats of a crystallographic plane distance “a”), while **iii** and **iv** are presumed to be too thick to observe such oscillations due to the limited resolution of the diffractometer used. By comparing the different momenta of the fringes, the crystalline thicknesses of **i** and **ii** were estimated to be 20 nm and 60 nm, respectively. The BFMO peak that is analogous to the STO 002 was further investigated via a reciprocal space map that is displayed for **i** in Fig. 1(b).

B. Atomic force microscopy

AFM was used to reveal the surface features of the films **i**, **ii**, **iii**, and **iv**. The initial image processing involved leveling by mean plane subtraction, aligning rows with a median method, and shifting the minimum height value to zero. These data are visualized as one-dimensional line-scans that integrate the vertical direction, as divided into four $1.25 \mu\text{m}$ regions, in Figs. 2(a) and 2(d) and as two-dimensional heat maps in Figs. 2(e)–2(h). Three types of features are seen in Fig. 2: (1) a wavy and connected surface characterized by the lateral coherence length (ξ) and surface roughness (σ), (2) small particulates on the surface that are characterized by their equivalent diameter (d_{particle}) and relative area compared to the total image area (A_{particle}), and (3) large chunks. Inflection points were seen in the height distribution function

due to the surface particulates, with values of 5.5 nm, 6.4 nm, 12.3 nm, and 15.2 nm, and due to the surface chunks, with values of 8.4 nm, 9.3 nm, 15.9 nm, and 18.8 nm, for films **i**, **ii**, **iii**, and **iv**, respectively. A height-height-correlation-function (HHCF)²⁴ that is a function of the lateral distance, r , was used to quantify the lateral coherence length, using a Gaussian such that

$$\text{HHCF}(r) = 2\sigma^2 \{1 - \exp[-(r/\xi)^2]\}, \quad (1)$$

where the maximum value of r was taken at $1 \mu\text{m}$ for fitting. The HHCF was calculated with thresholding to remove the contribution of the surface particles (to give σ , ξ), and without thresholding to remove the contribution of the surface particles (to give σ^* , ξ^*). The threshold cutoff was determined by manual inspection of the height profiles to remove the localized spikes due to surface particles or chunks. The analysis of the thresholded particulates was used to extract d_{particle} and A_{particle} . The results of these fittings are summarized in Table III. The large chunks did not occur frequently enough to allow quantitative analysis, but were typically in the range of 50 nm to 200 nm, and for the limited sampling available, they increased in size with film thickness.

C. X-ray reflectivity

XRR can determine the macroscopic interface parameters and depth dependent chemical composition via the scattering length densities that are probed through interactions of the X-rays with electrons. XRR shows the expected behavior of a total reflectance critical angle followed by a sharp decay at higher momentum transfers. For films **i** and **ii**, Kossel fringes are observed ($\Delta Q = 2\pi/d$ for a film of thickness “d”), while **iii** and **iv** are presumed too thick to observe such oscillations due to a limit of the resolution for this instrument, Fig. 3. The bare STO substrate was also measured, but is not shown. A rocking curve at finite momentum transfer shows the central specular peak and two diffuse scattering Yoneda wings that are characteristic of in-plane roughness and appear

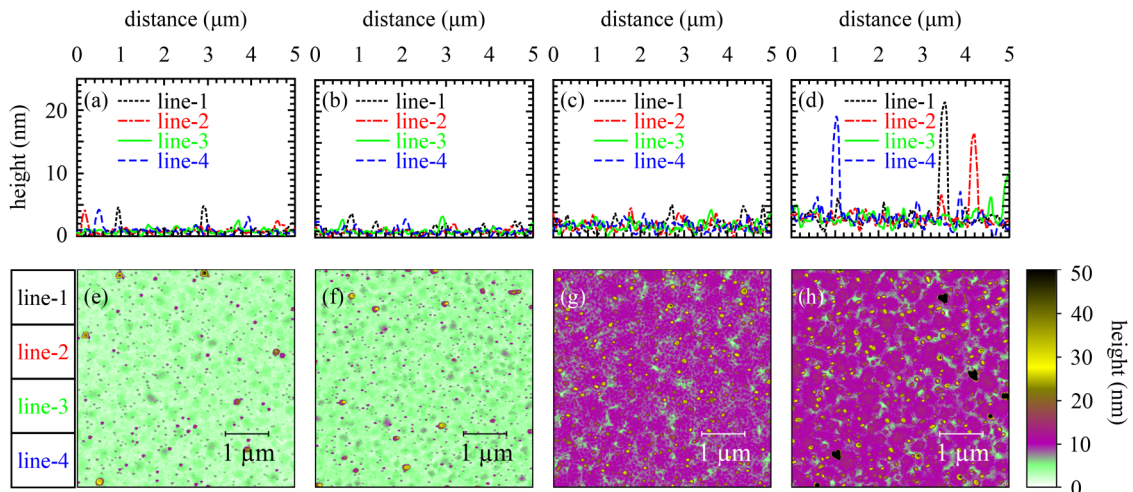


FIG. 2. AFM. All images have the same scale bar, where the sample identifier is as described in the text such that from left to right are **i**, **ii**, **iii**, and **iv**. The temperature is ambient.

TABLE III. AFM. Uncertainties of $\xi^{(*)}$ are around 1 nm, and on $\sigma^{(*)}$ are around 1 pm.

Sample ID	ξ (nm)	ξ^* (nm)	σ (nm)	σ^* (nm)	d_{particle} (nm)	A_{particle} (%)
i	65	73	1.0	2.1	15	1.3
ii	58	76	1.1	2.0	16	1.1
iii	54	53	1.6	3.3	33	7.8
iv	60	56	2.3	3.8	27	6.2

at positions, where the source or detector angle with respect to the sample surface equals the critical angle, as shown in the inset of Fig. 3. Films **i** and **ii** could be fit well with a single slab model to extract a film thickness, scattering length density (SLD), and roughness. Films **iii** and **iv** could not extract a thickness due to the absence of observable fringes, but scattering length density and roughness parameters could be extracted. The long period wave-vector discrepancies between experiments and fits could be reduced with additional model layers at the surface, but at the expense of additional parameters that may be masking subtleties of the background. For the STO substrate, the roughness could be fit to give a value of 0.6 nm. The results of the fits are shown in Table IV.

D. Polarized neutron reflectometry

PNR is sensitive to depth dependent nuclear composition and net magnetization perpendicular to the momentum transfer. The PNR was collected for the two films, **i** and **ii** that are of a thickness appropriate to the probe. Four cross sections were measured, R_{++} , R_{--} , R_{+-} , and R_{-+} , where the first two are non-spin-flip events, the second two are spin-flip events, and the sign symbols denote the neutron polarization directions. The spin-flip events, which are sensitive to magnetization orthogonal to the applied magnetic field that is in the plane of the film, were found to be negligible for these samples in this setup. For sample **i**, data were collected at 300 K and at 110 K, where 110 K was chosen, because it is above the structural phase transition of STO that can cause surface rumpling.²⁵ For sample **ii**, data were collected at 300 K and 110 K in a lower resolution and higher flux mode, and an additional 300 K data set was measured in a higher resolution and lower flux mode. Both samples **i** and **ii** show a splitting of the R_{++} and R_{--} cross sections that is due to net magnetization, and which is represented by the existence of spin asymmetry, $SA = (R_{++} - R_{--})/(R_{++} + R_{--})$, Figs. 4 and 5.

The simplest model for these data would be a mono-slab on the STO, and there is an approximate reproduction of the

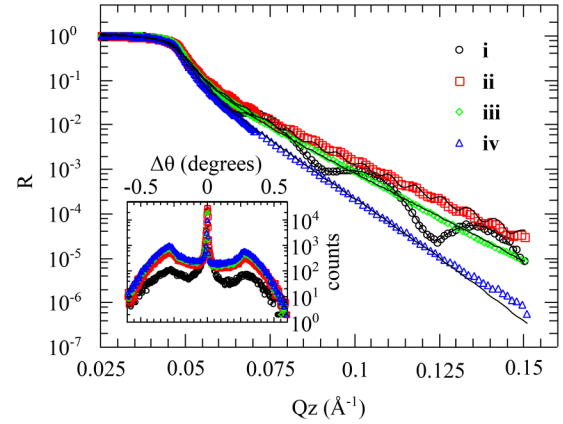


FIG. 3. XRR. The momentum dependence of the specular reflection at ambient temperature where symbols are experimental and overlaid lines are fits. (inset) Rocking curves at $Q_z = 0.0853 \text{ \AA}^{-1}$ at ambient temperature.

data for both films, Figs. 4 and 5. Some mono-slab fit parameters are shown in Table V.

For sample **i**, the crossing of R_{++} and R_{--} (zero crossing in the SA) cannot be reproduced with a homogeneous depth profile as for a mono-slab, but instead requires a different length scale for the nuclear and magnetic scattering. Tellingly, a tri-slab model allowing for magnetic and compositional changes at the interfaces may be refined to generate a zero crossing in the SA. In fact, the zero crossing is possible with a mono-slab nuclear scattering length density profile and a tri-slab magnetic scattering length density profile, but subtle changes in the nuclear part improve the fit. Additional layers beyond the tri-slab could subtly improve the model, but at the expense of overparameterization and model instability. For sample **ii**, the mono-slab model also has shortcomings in the reproduction of the magnetic scattering, but more qualitative features are reproduced than for **i**. The more complex tri-slab model whereby additional slabs at the STO to film and film to air interface are included is more quantitatively accurate for sample **ii** as well. The goodness of fit parameters of the various models and experimental conditions are summarized in Table VI. For both **i** and **ii**, it is found that there is larger magnetic scattering length density in the region of the STO to film interface that decreases toward the film to air interface. As the samples are cooled, the magnetization increases throughout the sample, but with a smaller increase near the surface than in the rest of the film. The thickness of the more magnetic phase is ≈ 10 nm, and for sample **i** it is ≈ 7 nm, while for sample **ii**, the relaxation is more gradual with an inflection closer to 20 nm. For sample **i**, the tri-slab model also shows a gradient in the nuclear scattering length density that is larger at the STO interface and

TABLE IV. XRR. The mean fit values are reported here as $\pm 1\sigma_{\text{STD}}$, as described in Sec. II.

Sample ID	Interface roughness (nm)	Thickness (nm)	Surface roughness (nm)	SLD (10^{-6} \AA^{-2})
i	0.85 ± 0.04	17.04 ± 0.03	1.54 ± 0.06	46.12 ± 0.17
ii	1.70 ± 0.07	73.75 ± 0.01	1.21 ± 0.01	46.46 ± 0.03
iii	1.492 ± 0.005	46.74 ± 0.01
iv	1.918 ± 0.001	46.09 ± 0.02

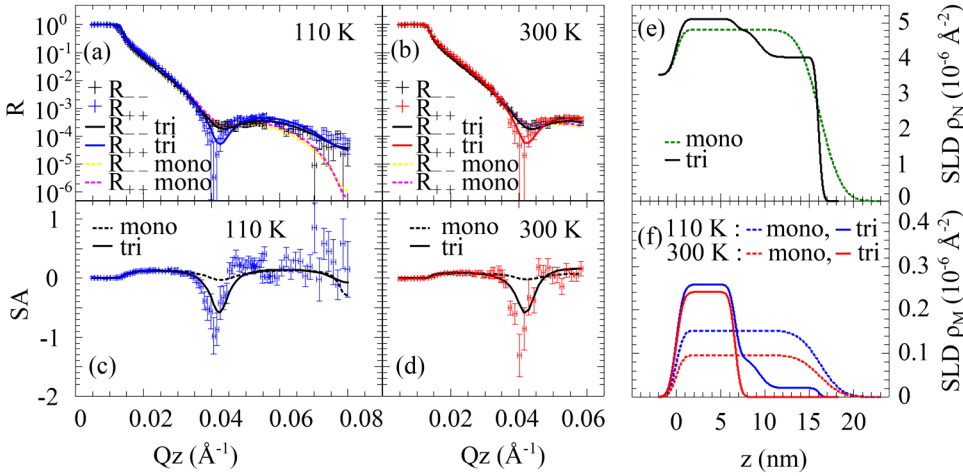


FIG. 4. PNR model of sample **i**. The momentum dependence of the specular reflection is shown for (a) 110 K and (b) 300 K. The spin asymmetry $[SA = (R_{++} - R_{--}) / (R_{++} + R_{--})]$ differently visualizes these data for (c) 110 K and (d) 300 K. The mono-slab and tri-slab models are both overlaid on the data, and the resulting (e) nuclear scattering length density (SLD ρ_N) profiles and (f) magnetic scattering length density (SLD ρ_M) profiles are shown. Uncertainty bars in counts come from normal statistics, and those in momentum are representative of the instrumental resolution.

decreases toward the air interface with a strong correlation to the magnetic phase. Such a chemical gradient is not required for the XRR data, which may be due to an increased sensitivity of the neutron experimental parameters or imply that the assertion of a chemical gradient is weak. For sample **ii**, the data are not sufficient to definitively make a statement on a potential nuclear scattering length gradient. Some tri-slab fit parameters are shown in Table VII.

E. X-ray photoelectron spectroscopy

XPS is a surface sensitive probe of chemical species, and films **i**, **ii**, **iii**, and **iv** were all measured. Survey and region scans are described in Sec. II. The degree of surface sensitivity may be estimated by considering the inelastic mean free path, which is calculated using the TPP-2M equation²⁶ and is shown in Fig. 6(a) for Ba_2FeMoO_6 . These mean free path estimations suggest that even from the thinnest film, sample **i**, the substrate is not probed. Survey scans, Fig. 6(b), were used to investigate the elemental composition, but the extracted values will be modulated by the surface concentrations and efficiency of the electron scattering process for a given moiety. Nevertheless, all observed peaks could be

assigned and the extracted elemental signals from Ba 3d, Sr 3d, Fe 2p, O 1s, and Mo 3d are shown in Table VIII. As anticipated, Ba, Fe, Mo, and O are all present, as is adventitious carbon, and in addition, Sr is present at the surface, while Ti is absent. Region scans were performed to further investigate the ions, Figs. 6(c)–6(f), and Ba 3d, O 1s, and Mo 3d all show two distinct species (Ba_1 , Ba_2 , O_1 , O_2 , Mo_1 , Mo_2), while Fe 2p only shows one species within the experimental resolution (Fe). Within the uncertainty, the expected branching ratios were observed, and the peak positions are shown in Table IX.

IV. DISCUSSION

Data have been presented in the Sec. III that shows the BFMO//STO films studied possess a degree of heterogeneity, which is not surprising given that the impetus of this work was to better understand the two magnetic ordering temperatures ($T_{C,1} > 300K$ and $T_{C,2} \approx 240 K$) reported for similarly prepared samples of BFMO//STO.⁵ The higher magnetic density region near the STO interface may be assigned to the $T_{C,1} > 300 K$ transition, while the lower magnetic density region near the air interface may be assigned to the $T_{C,2} \approx$

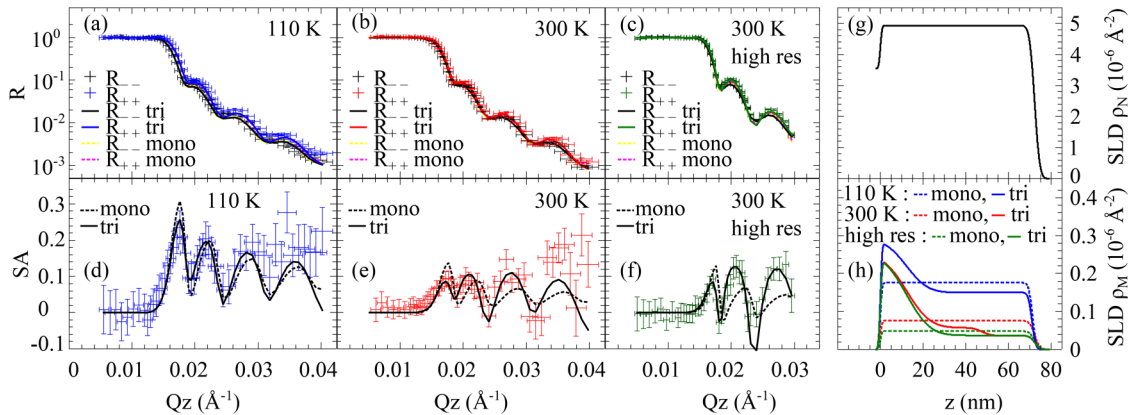


FIG. 5. PNR model of sample **ii**. The lower resolution, higher flux momentum dependence of the specular reflection is shown for (a) 110 K and (b) 300 K, and the higher resolution, lower flux data at (c) 300 K. The spin asymmetry $[SA = (R_{+-} - R_{-+}) / (R_{++} + R_{--})]$ differently visualizes these data for (d) 110 K, (e) 300 K, and (f) 300 K with high resolution. The mono-slab and tri-slab models are both overlaid on the data, and the resulting (g) nuclear scattering length density (SLD ρ_N) profiles and (h) magnetic scattering length density (SLD ρ_M) profiles are shown. Uncertainty bars in counts come from normal statistics, and those in momentum are representative of the instrumental resolution.

TABLE V. PNR mono-slab fit parameters. For the 300 K data of sample **ii**, the high resolution data are in parentheses. The mean fit values are reported here as $\pm 1\sigma_{\text{STD}}$, as described in Sec. II.

Sample ID	Thickness (nm)	Surface roughness (nm)	$\rho_{\text{N}} (10^{-6} \text{ \AA}^{-2})$	$\rho_{\text{M}} (10^{-6} \text{ \AA}^{-2})$ 110 K	$\rho_{\text{M}} (10^{-6} \text{ \AA}^{-2})$ 300 K
i	16.23 \pm 0.04	1.92 \pm 0.02	4.824 \pm 0.005	0.152 \pm 0.003	0.096 \pm 0.008
ii	72.2 \pm 0.01	1.8 \pm 0.2	4.928 \pm 0.006	0.17 \pm 0.01	0.076 \pm 0.005(0.048 \pm 0.005)

240 K transition. In the following, we attempt to unify the data to describe the surface features, the chemical characteristics of the film, and the magnetic characteristics of the film.

These BFMO//STO films are mainly crystalline. The XRD showed a pseudo-perovskite phase that has an elongated lattice constant out of the plane that increases with film thickness, and previous work on films by the same group under identical growth conditions have shown registered epitaxy.⁵ The changing lattice constant with film thickness suggests a depth dependent strain in the films. The Laue and Kiessig fringes gave similar thicknesses for the films thin enough to resolve (**i** and **ii**), showing that the preponderance of the film is one crystalline structure. No extra phases were seen with XRD, which means that any additional possible phases would be a significantly lesser volume and likely randomly oriented, whereby the diffracted beams are less concentrated in the solid angle. Grossly, the XPS of **i**, **ii**, **iii**, and **iv** all showed that there are Sr, Ba, Fe, Mo, and O present at the surface of the films. Sr is not present in the target and must diffuse from the substrate to the film during PLD. This type of A-site mixing of film and substrate has been seen in PLD of SrRuO₃ and Pr_{0.7}Ca_{0.3}MnO₃²⁷ and LaCrO₃ on SrTiO₃.²⁸

There are surface features on these films. AFM shows a connected film of nanometer roughness (as does reflectivity) that is coated by hundred nanometer chunks and tens of nanometer particulates. The surface sensitive XPS showed at least two chemical species being present for Ba, O, and Mo. Therefore, it is likely that the surface objects belong to a different crystal structure than the surface of the crystalline film that leaves the two phases immiscible. At higher oxygen pressures than used here, BaMoO₄ was seen in XRD of BFMO//STO,⁵ and SrMoO₄ was seen in XRD of SFMO//STO.²⁹ Fe₃O₄ and elemental Fe were also observed in SFMO//STO XRD for higher vacuum environments.²⁹ While

BaMoO₄ is not observed in the XRD of **i**, **ii**, **iii**, and **iv**, there is evidence for its presence in the XPS. BaMoO₄ is reported to have Ba²⁺3d_{5/2} = 779.1 eV, Mo⁶⁺3d_{5/2} = 232.2 eV, and O²⁻1s = 531.0 eV,³⁰ which are respectively near Ba₁ or Ba₂, Mo₁, and O₂, respectively. The Mo₂ peak would then correspond to Mo⁵⁺ as in BFMO. The O₁ = 529.7 eV O1s signal is a perovskite peak that is present in CaTiO₃ and BaTiO₃ (BTO), and the BTO peak for Ba3d_{5/2} = 779.0 eV is near Ba₁ and Ba₂.³¹

The data show a non-trivial chemical make-up in the crystalline film phase. Previously, BFMO//STO chemical analysis by energy-dispersive X-ray spectroscopy on a scanning tunneling electron microscope did not identify off-stoichiometry of Mo:Fe from 1 : 1, but no quantities were reported, and the temperature dependence of the resistivity in that report⁵ was consistent with an Fe-rich material.⁷ Similarly, for a study of SFMO//STO, no off-stoichiometry of the B-site was identified, but no quantities were reported.²⁹ For the film phase, the reflectivity studies provide chemical information. The neutron and X-ray scattering lengths arise from different interactions and therefore the potential for different elemental contrast, which is achieved in this instance, Table X. Using the unit cell parameters from XRD, a connection between chemical formula and scattering length density is possible. For a formula of Ba₂FeMoO₆, $\rho_{\text{N,neutron}} = 4.99 \times 10^{-6} \text{ \AA}^{-2}$ and $\rho_{\text{X-ray}} = 51.78 \times 10^{-6} \text{ \AA}^{-2}$ (for sample **i** unit cell parameters) and experimentally for sample **i**, $\rho_{\text{N,neutron}} = 5.118 \times 10^{-6} \text{ \AA}^{-2}$ at the STO interface, $\rho_{\text{N,neutron}} = 4.04 \times 10^{-6} \text{ \AA}^{-2}$ at the air interface, and $\rho_{\text{X-ray}} = 46.12 \times 10^{-6} \text{ \AA}^{-2}$, while for sample **ii**, $\rho_{\text{N,neutron}} = 4.933 \times 10^{-6} \text{ \AA}^{-2}$ and $\rho_{\text{X-ray}} = 46.46 \times 10^{-6} \text{ \AA}^{-2}$. Qualitatively, the undershooting of $\rho_{\text{X-ray}}$ compared to that expected for pure BFMO suggests that Fe and Sr are likely richer than the ideal case, and similar arguments can be made for the relative values of $\rho_{\text{N,neutron}}$. Quantitatively, taking a chemical formula parameterized with three variables of Sr_{2-y}Ba_yFe_{1+x}Mo_{1-x}O_{6-z}, it is possible to co-fit the chemical formula to the experimentally determined $\rho_{\text{N,neutron}}$ and $\rho_{\text{X-ray}}$. At the STO interface, these fits give Ba_{0.98}Sr_{1.02}Fe_{1.29}Mo_{0.71}O_{5.78} for film **i** and Ba_{1.14}Sr_{0.86}Fe_{1.19}Mo_{0.81}O_{5.48} for film **ii**. At the film surface, the sample **ii** data did not refine a different SLD for these data, while the data point at the terminal surface for sample **i** gives Ba_{2.00}Sr_{0.00}Fe_{1.40}Mo_{0.60}O_{3.81} but the meaning of such numbers within the experimental uncertainty is unclear. Similarly, normalizing the XPS to the two A-sites yields Sr_{1.18}Ba_{0.82}, Sr_{1.35}Ba_{0.65}, Sr_{1.26}Ba_{0.74}, and Sr_{1.22}Ba_{0.78}, while for the B-sites, a similar scaling gives Fe_{1.31}Mo_{0.69}, Fe_{1.38}Mo_{0.62}, Fe_{1.32}Mo_{0.68}, and Fe_{1.64}Mo_{0.36} for films **i**, **ii**, **iii**, and **iv**, respectively. The strontium present in XPS at the surface in film **i** seems to suggest that the films have a degree of chemical homogeneity and strontium leeches through the entire

TABLE VI. Goodness of fit improvement for tri-slab model versus mono-slab model.

Sample ID	Condition	Model	χ^2	U _{SA}
I	300 K	Tri-slab	15.0	0.57
		Mono-slab	16.0	0.80
	110 K	Tri-slab	42.5	0.61
		Mono-slab	44.3	0.76
ii	300 K—high res.	Tri-slab	5.5	0.30
		Mono-slab	7.0	0.74
	300 K	Tri-slab	4.6	0.48
		Mono-slab	4.6	0.60
	110 K	Tri-slab	3.9	0.28
		Mono-slab	6.5	0.33

TABLE VII. PNR tri-slab fit parameters.

Sample ID	Thickness (nm)	Surface roughness (nm)	ρ_N (10^{-6} \AA^{-2}), STO interface	ρ_N (10^{-6} \AA^{-2}), air interface	ρ_M (10^{-6} \AA^{-2}), 110 K, STO interface	ρ_M (10^{-6} \AA^{-2}), 110 K, air interface	ρ_M (10^{-6} \AA^{-2}), 300 K, STO interface	ρ_M (10^{-6} \AA^{-2}), 300 K, air interface
i	15.9 ± 0.4	0.40 ± 0.06	5.11 ± 0.04	4.04 ± 0.05	0.26 ± 0.03	0.02 ± 0.03	0.241 ± 0.017	0.000 ± 0.009
ii	72 ± 1	1.4 ± 0.3		4.93 ± 0.01	0.3 ± 0.1	0.15 ± 0.05	0.25 ± 0.01	0.04 ± 0.01

film **i**. Along these lines, the similar XPS derived surface strontium concentrations for films that are 17 nm (as determined from reflectivity for sample **i**) and up to ≈ 300 nm (as estimated from XRD intensity and number of deposition cycles for sample **iv**) suggest an approximately uniform strontium concentration throughout, although there may be a subtler concentration gradient that is beyond these data. The XRD unit cell parameters may also give some insight into the chemical formula in a less quantitative way. One potential issue when attempting to use XRD as an elemental analyst for BFMO is the multiple oxidation states that may be present and change with stoichiometry. For example, BFMO is considered to be $\text{Ba}_2^+\text{Fe}^{3+}\text{Mo}^{5+}\text{O}_6^{2-}$, and if the end members are $\text{Ba}^{2+}\text{Fe}^{4+}\text{O}_3^{2-}$ ($a_{\text{BaFeO}_3} = 3.971 \text{ \AA}$ ³²) and $\text{Ba}^{2+}\text{Mo}^{4+}\text{O}_3^{2-}$ ($a_{\text{BaMoO}_3} = 4.040 \text{ \AA}$ ³³), then the oxidation states must change on the transition metals for different stoichiometries that will in turn affect the bond lengths. Qualitatively, $x > 0$ ($y < 0$) will reduce the unit cell volume and $x < 0$ ($y > 0$) will increase the unit cell volume. Oxygen off-stoichiometry

may reduce the unit cell volume in both cases, as oxygen rich formulas are typically realized as A-site vacancies.¹⁵ In SFMO deposited via PLD, such a deficiency of the alkaline earth metal was seen.²⁹ Alternatively, for the isoelectronic A-site substitution in $\text{Sr}_y\text{Ba}_{1-y}\text{FeMoO}_6$, Vegard's law of averages is expected to approximately hold as in $\text{Sr}_y\text{Ba}_{1-y}\text{MoO}_3$ ³³ and $\text{Sr}_y\text{Ba}_{2-y}\text{FeMoO}_6$.³⁴ The cube-root of the single-perovskite unit cell volumes (V) of **i**, **ii**, **iii**, and **iv** may be calculated using the $a_{\text{STO}} = 3.90 \text{ \AA}$ for the in-plane lattice constants and the out-of-plane lattice constants in Table II to yield $V_{\text{i}}^{1/3} = 3.943 \text{ \AA}$, $V_{\text{ii}}^{1/3} = 3.944 \text{ \AA}$, $V_{\text{iii}}^{1/3} = 3.947 \text{ \AA}$, and $V_{\text{iv}}^{1/3} = 3.946 \text{ \AA}$, respectively. For BFMO, $V_{\text{BFMO}}^{1/3} = 4.031 \text{ \AA}$, which is significantly larger than the $V_{\text{STO}}^{1/3} = 3.90 \text{ \AA}$ ³⁵ of the substrate, resulting in an even worse match than for SFMO//STO, as $V_{\text{SFMO}}^{1/3} = 3.949 \text{ \AA}$.¹ For $y \approx 1$, as in the reflectivity fits, $V_{y \approx 1}^{1/3} = 3.990 \text{ \AA}$, and from the Fe doping experiments on SFMO, there would also be a decrease in lattice parameter for $x > 0$.³⁶ In the synthesis paper of BFMO//STO, it was found that increasing the growth temperature from $600 \text{ }^\circ\text{C}$ to

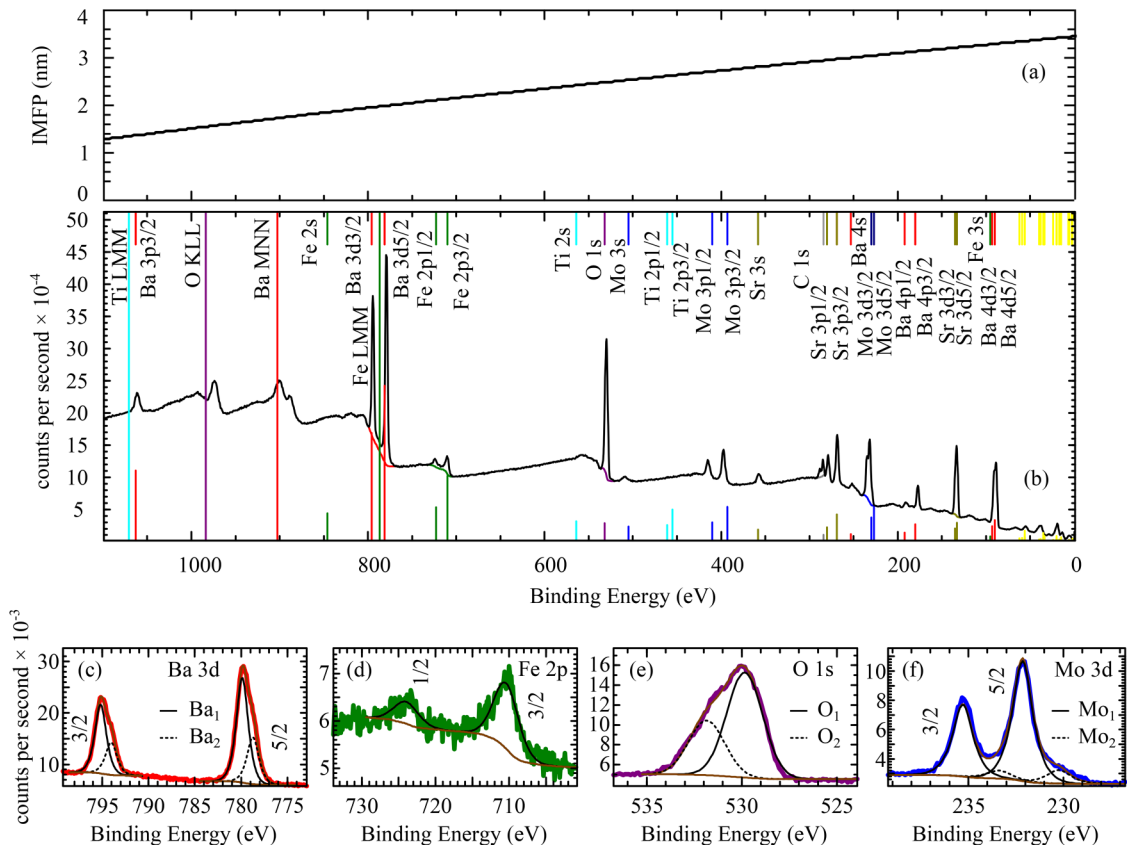


FIG. 6. XPS. (a) The inelastic mean free path (IMFP) of $\text{Ba}_2\text{FeMoO}_6$. (b) An example of a survey scan from sample **i** is shown. Example region scans from sample **iv** for (c) Ba 3d, (d) Fe 2p, (e) O 1s, and (f) Mo 3d are shown.

TABLE VIII. The elemental percentages segregated into resolved chemical species from the XPS.

	Sr (%)	Ba ₁ (%)	Ba ₂ (%)	Fe (%)	Mo ₁ (%)	Mo ₂ (%)	O ₁ (%)	O ₂ (%)
i	13.2	5.9	3.2	4.6	6.8	2.4	32.9	31.0
ii	12.9	6.2	2.8	4.9	6.8	2.2	33.5	30.7
iii	11.7	4.8	2.1	3.3	6.1	1.7	32.6	37.7
iv	13.3	6.1	2.5	5.0	8.4	1.1	41.8	21.8

900 °C (in 100 °C increments) monotonically decreased the out of plane lattice constant,⁵ suggesting that there may be an annealing toward a ground state with a smaller film unit cell volume. Here, the out of plane lattice constant generally increases with thickness, although the repetition rate of the laser also changes, so it is unclear which effect might dominate, but in both cases, this would suggest that in the vicinity of the substrate, there is a tendency to have a reduced lattice constant. These interfacial lattice constant considerations illustrate a possible force driving the Sr to Ba and Mo to Fe chemical concentrations.

Just as the film may be affected by the substrate, the film deposition may also induce changes in the surface of the substrate at the interface. We have presented evidence that the source of the strontium that is diffused to the deposited films, from a Ba₂FeMoO₆ target, must be from the SrTiO₃ substrate. This cation diffusion of strontium into the PLD films that SrTiO₃ may transform to Sr_αBa_βTiO₃ near the interface. Previously, we referenced the cubic a_{STO} = 3.90 Å, and while the BTO is tetragonal at room temperature (a = 3.9998 Å, c = 4.0180 Å), the a_{BTO} = 4.006 Å pseudo-cubic lattice parameter may be used to compare and is more than 2% larger than a_{STO}. Diffusion of the alkaline earth metal cations across the interface into the substrate would reduce the strain between substrate and deposited film, and there are data consistent with such a process. The XRR and PNR data may be considered in the context of a more complex model that allows a substrate interface layer; such complex models may be problematic due to the potential for non-uniqueness. The XRR fits presented in Sec. III C are robust to give the mono-slab thickness with a well determined parameter set. Due to the length scales probed, this effect of a discrete substrate surface modification is clearest in sample **i**. A new model (mono-slab*) includes an additional slab at the substrate to film interface and an additional slab at the film to air interface, Fig. S1 in the [supplementary material](#). For the mono-slab model, $\chi^2 = 4.62$, and this is decreased to $\chi^2 = 1.30$ in the mono-slab* model. The additional slab at the film to air interface has no appreciable effect, while the slab at the substrate to film interface refines to a thickness of 2.92 ± 0.03 nm, with an SLD of $42.95 \pm 0.05 \times 10^{-6} \text{ \AA}^{-2}$. For reference, the SLD of STO is $39.7 \times 10^{-6} \text{ \AA}^{-2}$ and the SLD of BTO is

$44.4 \times 10^{-6} \text{ \AA}^{-2}$, as calculated from their crystallographic parameters,^{35,37} where the dominant factor in these different SLDs is due to the number of electrons, and a secondary factor is the lattice constants changing. The mono-slab* model film has an SLD of $44.73 \pm 0.03 \times 10^{-6} \text{ \AA}^{-2}$ (versus $46.12 \pm 0.17 \times 10^{-6} \text{ \AA}^{-2}$ for the mono model). A similar complexification is possible for the PNR tri-slab model, to have a tri-slab* model that allows for the substrate STO to change SLD as an additional parameter. These PNR tri-slab* fits tend toward $3.2 \times 10^{-6} \text{ \AA}^{-2}$ at the film to STO interface, which is between $3.5 \times 10^{-6} \text{ \AA}^{-2}$ for STO and $3.0 \times 10^{-6} \text{ \AA}^{-2}$ for BTO, and the resulting magnetic profiles are changed by less than 10% for such a modification.

The magnetism in the films is inhomogeneous and may be connected to structural and chemical inhomogeneity. To put these BFMO//STO films in the context of the literature, the ρ_M magnetic scattering length density may be converted to μ_B by using the lattice constants determined with XRD and the magnetic scattering amplitude for one μ_B , $\rho_{MAG} = 2.695 \text{ fm}$,³⁸ Table XI. For double-perovskites in general, the dominant factor reducing the net magnetic moment is typically the anti-site defects, whereby Mo and Fe sites here would swap, and the saturation magnetization (M_{SAT}) is approximately linear in the chemical order parameter without affecting T_C ,¹³ but other factors may contribute. The observation of Sr in the films suggests that A-site doping may play a role in the magnetic response. One study of Sr_{2-y}Ba_yFeMoO₆ using solid state synthesis found a non-linear, monotonic interpolation of T_C 's between 420 K for $y = 0$ and 300 K for $y = 2$, with M_{SAT} measured at 80 K linearly varying between $2.1 \mu_B/\text{f.u.}$ (f.u. = the double perovskite formula unit) for $y = 0$ and $3.0 \mu_B/\text{f.u.}$ for $y = 2$.³⁴ A similar dependence of T_C upon Ba/Sr content was seen in a study of magnetocaloric effects in Sr doped Ba₂FeMoO₆.³⁹ Another report found an enhancement of the T_C of Sr_{2-y}Ba_yFeMoO₆ for $y = 0.4$, before a decrease in T_C was observed,⁴⁰ and still another study found that there was no effect on T_C for up to $y = 1.0$, after which the T_C increased,⁴¹ and in both studies, M_{SAT} also increased with barium content. So, the Sr enrichment can increase T_C , but is not expected to alter the M_{SAT} . Conversely, iron doping up to $x = 0.25$ (the maximum reported) was found to have little to no effect on T_C , but

TABLE IX. Spectroscopic positions from XPS regions scans.

	Ba ₁ 3d _{5/2}	Ba ₂ 3d _{5/2}	Fe 2p _{3/2}	Mo ₁ 3d _{5/2}	Mo ₂ 3d _{5/2}	O ₁ 1s	O ₂ 1s
Peak (eV)	779.8	778.6	710.3	232.0	230.1	529.7	531.7
Δ (eV)		15.3	13.5		3.15		

TABLE X. Coherent neutron scattering lengths, b_N , used for neutron SLD calculation and the Z number that is the dominant factor in the x-ray SLD.

Element	b_N (fm)	Z
Sr	7.02	38
Ba	5.07	56
Fe	9.45	26
Mo	6.715	42
O	5.803	8

linearly decreased M_{SAT} from $3.3 \mu_B/f.u.$ at $x=0$ to $2.3 \mu_B/f.u.$ at $x=0.25$.³⁶ Oxygen deficiency, as is seen here in the scattering length density model calculations, is expected for the low oxygen partial pressures used during synthesis, and for SFMO a decrease of 7% oxygen in the formula unit decreased M_{SAT} from $3.57 \mu_B/f.u.$ to $3.30 \mu_B/f.u.$, accompanied by subtle change in lattice constants (shrinking c but growing a to have $<0.1\%$ volume increase).⁴² For a phase to have $T_C \approx 240$ K as in the BFMO//STO films near the surface, it is then most likely that finite size effects and grains come into play, and these microstructural effects would also affect the M_{SAT} for that region. Indeed, the AFM showed lateral structural coherence lengths at the surface to be ≈ 60 nm for films **i**, **ii**, **iii**, and **iv**, and a 5% barium doping of sol-gel synthesized Sr_2FeReO_6 found a reduction in M_{SAT} (by a factor of ≈ 3) and T_C as the grain sizes were reduced from 80–800 nm for the undoped with a wide distribution to 80–180 nm for the 5% barium doped with a tight distribution near 120 nm.⁴³ Additional work will be required if quantitative microstructural models are to be applied to this system. Finally, while there may be interface effects due to magnetic proximity,⁴⁴ these films seem to have their magnetic inhomogeneity connected to chemical and structural effects.

This section has made attempts to extract chemical and magnetic inhomogeneities by invoking a suite of probes, resulting in an array of extracted numbers. The possibility of unknown and systemic experimental uncertainties may limit quantitative comparison of these numbers. Some examples of uncertainties are that the scattering length density calculations are subject to changes in electron density and lattice constant changes (both of which may vary in the films in ways beyond the ability of these probes to interrogate), that the XPS relative sensitivity factors may be modified in the film matrix, as compared to the standards, that the sampling of microscopes like AFM may not be macroscopic in scope, and that subtle alignments can affect the scattering probes. On the other hand, there is a clear consistency to the results that have been discussed in this section.

TABLE XI. Magnetic SLD, ρ_M , converted to $\mu_B/f.u.$

Sample ID	M ($\mu_B/f.u.$) 110 K, STO interface	M ($\mu_B/f.u.$) 110 K, air interface	M ($\mu_B/f.u.$) 300 K, STO interface	M ($\mu_B/f.u.$) 300 K, air interface
i	1.18	0.09	1.10	0.00
ii	1.32	0.68	1.15	0.17

V. CONCLUSIONS

In summary, we have presented data that progress the understanding of differences between BFMO powders and BFMO films on STO substrates. The out-of-plane lattice constant of BFMO//STO via XRD increases with film thickness from 4.040 \AA for **i** (17 nm thick) to 4.034 \AA for **ii** (74 nm thick) to 4.044 \AA for **iii** (≈ 200 nm thick), and then decreases to 4.041 \AA for **iv** (≈ 300 nm to ≈ 400 nm thick) versus 3.90 \AA for STO and 4.031 \AA for powder BFMO. Films **i** and **ii** that are appropriate for PNR have a region of higher T_C and M_{SAT} near the substrate interface (up to 7 nm and 20 nm from the interface, respectively) compared to the rest of the film and this temperature dependent magnetic depth profile explains the reported SQUID magnetometry observation of $T_{C,1} > 300$ K and $T_{C,2} \approx 240$ K. Strontium of similar concentrations that is not present in the BFMO deposition target and $Fe/Mo > 1$ is observed via XPS within nanometers of the surface for all films, while neutron and X-ray reflectivity in concert for **i** and **ii** show similar strontium uptake and $Fe/Mo > 1$ at the STO interface. Two Ba and O species are observed in XPS within nanometers of the surface, where one is from the double-perovskite and the other from a $BaMoO_4$ phase, and this $BaMoO_4$ may be present as the particulates observed in the AFM. The lateral structural coherence length via AFM is ≈ 60 nm for all films at the surface.

And so, a semi-quantitative unified picture of BFMO//STO emerges that explains the previously puzzling decreased character of the magnetization measurements that suppressed M_{SAT} and had a majority phase of $T_C (< T_{C,powder}) = 240$ K. $BaMoO_4$ may precipitate out during PLD, leaving some remnants at the film surface as particulates and causing a Ba and Mo deficiency in the epitaxial film. The observation of Sr in the films was surprising, may help explain the non-monotonic magnetoresistance previously observed in BFMO//STO, and will be important to consider for similar (double) perovskites where a strain is present that may be relaxed via interstitial cation diffusion from the substrate. Within 10 nm to 20 nm of the STO interface where larger T_C and M_{SAT} is observed, the substrate may stabilize larger structural coherence lengths than the observed surface grains that may subdue T_C and M_{SAT} , but no data are available to quantify that aspect. The changing lattice constant with thickness suggests a depth dependent strain in the films, which has a lesser known effect. Iron richness, anti-site disorder, and oxygen vacancies may also conspire to affect the properties. These considerations will be essential to inform substrate choice in future BFMO applications.

SUPPLEMENTARY MATERIAL

See [supplementary material](#) for an XRR model including an additional substrate parameter.

ACKNOWLEDGMENTS

The authors gratefully acknowledge the Summer Undergraduate Research Fellowship at the National Institute of Standards and Technology (NIST) Center for Neutron

Research for Lisa J. Kraye, the financial support provided by NIST and the Center for High Resolution Neutron Scattering, and the usage of facilities supported, in part, by the National Science Foundation under Agreement No. DMR-0944772. Daniel M. Pajerowski is supported through the Scientific User Facilities Division of the Department of Energy (DOE) Office of Science, sponsored by the Basic Energy Science (BES) Program, DOE Office of Science.

Certain commercial equipment, instruments, or materials are identified in this paper to foster understanding. Such an identification does not imply recommendation or endorsement by the National Institute of Standards and Technology, nor does it imply that the materials or equipment identified are necessarily the best available for the purpose. This manuscript has been authored by UT-Battelle, LLC under Contract No. DE-AC05-00OR22725 with the U.S. Department of Energy. The United States Government retains and the publisher, by accepting the article for publication, acknowledges that the United States Government retains a non-exclusive, paid-up, irrevocable, world-wide license to publish or reproduce the published form of this manuscript, or allow others to do so, for United States Government purposes. The Department of Energy will provide public access to these results of federally sponsored research in accordance with the DOE Public Access Plan (<http://energy.gov/downloads/doi-public-access-plan>).

- ¹R. P. Borges, R. M. Thomas, C. Cullinan, J. M. D. Coey, R. Suryanarayanan, L. Ben-Dor, L. Pinsard-Gaudart, and A. Revcolevschi, *J. Phys. Condens. Matter* **11**, L445 (1999).
- ²M. I. Katsnelson, V. Y. Irkhin, L. Chioncel, A. I. Lichtenstein, and R. A. De Groot, *Rev. Mod. Phys.* **80**, 315 (2008).
- ³H. Han, B. J. Han, J. S. Park, B. W. Lee, S. J. Kim, and C. S. Kim, *J. Appl. Phys.* **89**, 7687 (2001).
- ⁴W. Zhong, N. J. Tang, C. T. Au, and Y. W. Du, *IEEE Trans. Magn.* **43**, 3079 (2007).
- ⁵K.-W. Kim, S. Ghosh, S. Buvaev, S. Mhin, J. L. Jones, A. F. Hebard, and D. P. Norton, *J. Appl. Phys.* **112**, 083923 (2012).
- ⁶L. R. Moras, *J. Inorg. Nucl. Chem.* **36**, 3876 (1974).
- ⁷D. Serrate, J. M. De Teresa, and M. R. Ibarra, *J. Phys. Condens. Matter* **19**, 1 (2007).
- ⁸K. I. Kobayashi, T. Kimura, H. Sawada, K. Terakura, and Y. Tokura, *Nature* **395**, 677 (1998).
- ⁹H. Asano, S. B. Ogale, J. Garrison, A. Orozco, Y. H. Li, E. Li, V. Smolyaninova, C. Galley, M. Downes, M. Rajeswari, R. Ramesh, and T. Venkatesan, *Appl. Phys. Lett.* **74**, 3696 (1999).
- ¹⁰A. S. Ogale, S. B. Ogale, R. Ramesh, and T. Venkatesan, *Appl. Phys. Lett.* **75**, 537 (1999).
- ¹¹R. P. Borges, S. Lhostis, M. A. Bari, J. J. Versluijs, J. G. Lunney, J. M. D. Coey, M. Besse, and J. P. Contour, *Thin Solid Films* **429**, 5 (2003).
- ¹²H. Asano, Y. Kohara, and M. Matsui, *Jpn J. Appl. Phys.* **41**, L1081 (2002).

- ¹³S. Colis, D. Stoeffler, C. Mny, T. Fix, C. Leuvrey, G. Pourroy, A. Dinia, and P. Panissod, *J. Appl. Phys.* **98**, 033905 (2005).
- ¹⁴D. Stoeffler and S. Colis, *J. Phys. Condens. Matter* **17**, 6415 (2005).
- ¹⁵J. A. M. van Roosmalen and E. H. P. Cordfunke, *J. Solid State Chem.* **110**, 109 (1994).
- ¹⁶J. F. Ankner and G. P. Felcher, *J. Magn. Magn. Mater.* **200**, 741 (1999).
- ¹⁷Y. Liu, J. M. Lucy, A. Glavic, H. Ambaye, V. Lauter, F. Y. Yang, and S. G. E. Te Velthuis, *Phys. Rev. B Condens. Matter Mater. Phys.* **90**, 2 (2014).
- ¹⁸N. Maskil and M. Deutsch, *Phys. Rev. A* **38**, 3467 (1988).
- ¹⁹J. A. Bearden, *Rev. Mod. Phys.* **39**, 78 (1967).
- ²⁰D. Nečas and P. Klapetek, *Cent. Eur. J. Phys.* **10**, 181 (2012).
- ²¹J. A. Dura, D. J. Pierce, C. F. Majkrzak, N. C. Maliszewskij, D. J. McGillivray, M. Lösche, K. V. O'Donovan, M. Mihailescu, U. Perez-Salas, D. L. Worcester, and S. H. White, *Rev. Sci. Instrum.* **77**, 074301 (2006).
- ²²B. J. Kirby *et al.* *Current Opinion in Colloid & Interface Science* **17**, 44–53 (2014).
- ²³B. J. Kirby, P. A. Kienzle, B. B. Maranville, N. F. Berk, J. Krycka, F. Heinrich, and C. F. Majkrzak, *Curr. Opin. Colloid Interface Sci.* **17**, 44 (2012).
- ²⁴D. Nečas and P. Klapetek, *Ultramicroscopy* **124**, 13 (2013).
- ²⁵S. Singh, T.-Y. Chien, J. R. Guest, and M. R. Fitzsimmons, *Phys. Rev. B* **85**, 115450 (2012).
- ²⁶S. Tanuma, C. J. Powell, and D. R. Penn, *Surf. Interface Anal.* **17**, 927939 (1991).
- ²⁷R. Hillebrand, E. Pippel, I. Vrejoiu, and D. Hesse, *Phys. Status Solidi* **211**, 536 (2014).
- ²⁸L. Qiao, K. H. L. Zhang, M. E. Bowden, T. Varga, V. Shutthanandan, R. Colby, Y. Du, B. Kabius, P. V. Sushko, M. D. Biegalski, and S. A. Chambers, *Adv. Funct. Mater.* **23**, 2953 (2013).
- ²⁹J. Santiso, A. Figueras, and J. Fraxedas, *Surf. Interface Anal.* **33**, 676 (2002).
- ³⁰J. Bi, D. Q. Xiao, D. J. Gao, P. Yu, G. L. Yu, W. Zhang, and J. G. Zhu, *Cryst. Res. Technol.* **38**, 935 (2003).
- ³¹C. Blanco, G. Fourlaris, B. Rand, and F. L. Riley, *J. Am. Ceram. Soc.* **86**, 1777 (1999).
- ³²N. Hayashi, T. Yamamoto, H. Kageyama, M. Nishi, Y. Watanabe, T. Kawakami, Y. Matsushita, A. Fujimori, and M. Takano, *Angew. Chemie Int. Ed.* **50**, 12547 (2011).
- ³³L. H. Brixner, *J. Inorg. Nucl. Chem.* **14**, 225 (1960).
- ³⁴A. H. Habib, A. Saleem, C. V. Tomy, and D. Bahadur, *J. Appl. Phys.* **97**, 10A906 (2005).
- ³⁵T. Yamanaka, N. Hirai, and Y. Komatsu, *Am. Mineral.* **87**, 1183 (2002).
- ³⁶D. Topwal, D. D. Sarma, H. Kato, Y. Tokura, and M. Avignon, *Phys. Rev. B* **73**, 094419 (2006).
- ³⁷R. H. Buttner and E. N. Maslen, *Acta Crystallogr. B* **B48**, 764 (1992).
- ³⁸G. Shirane, S. Shapiro, and J. Tranquada, *Neutron Scattering with a Triple-Axis Spectrometer* (Cambridge University Press, Cambridge, 2004).
- ³⁹I. Hussain, M. S. Anwar, S. N. Khan, A. Shahee, Z. Ur Rehman, and B. Heun Koo, *Ceram. Int.* **43**, 10080 (2017).
- ⁴⁰X. M. Feng, G. H. Rao, G. Y. Liu, W. F. Liu, Z. W. Ouyang, and J. K. Liang, *Solid State Commun.* **129**, 753 (2004).
- ⁴¹E. K. Hemery, G. V. M. Williams, and H. J. Trodahl, *Phys. B Condens. Matter* **390**, 175 (2007).
- ⁴²J. Töpfer, R. Kirchseisen, and S. Barth, *J. Appl. Phys.* **105**, 07D712 (2009).
- ⁴³T. Yamakoshi, K. Nomura, T. Kitamori, J. Shimoyama, Z. Nemeth, and Z. Homonnay, *Hyperfine Interact.* **191**, 405 (2009).
- ⁴⁴P. K. Manna and S. M. Yusuf, *Phys. Rep.* **535**, 61 (2014).